Differential photoelectron holography

Differential photoelectron holography

T-C Chiang

Department of Physics, University of Illinois at Urbana-Champaign, 1110 West Green Street, Urbana, IL 61801-3080, USA
and
Frederick Seitz Materials Research Laboratory, University of Illinois at Urbana-Champaign, 104 South Goodwin Avenue, Urbana, IL 61801-2902, USA

Abstract
Atoms near a selected surface atomic site can be imaged in three dimensions by photoelectron holography. The experiment involves acquiring hundreds or thousands of angle-resolved photoemission spectra from a core level of the selected atomic site over a wide range of photon energy and for a large number of emission directions. For good image quality, the precision of the intensity measurement must be better than $\sim$1% over the entire data set, but this is difficult to achieve. Two methods based on differential measurements that allow intensity self-normalization are presented here as a solution. One method is based on measurements of intensity branching ratios between spin–orbit-split core level peaks, and the other is based on measurements of logarithmic derivatives of the intensity function. These methods are illustrated by two examples, As-terminated Si(1 1 1) and Bi-terminated Si(1 1 1). The As/Si(1 1 1) results are in excellent agreement with the accepted structure of the system, thus verifying the efficacy of the methods. The Bi/Si(1 1 1) results resolve a long-standing controversy regarding the correct structure of this system.

1. Introduction

Photoelectron holography is a direct method for surface atomic structure determination [1–15]. Experimentally, a large set of angle-resolved photoemission data is taken over wide ranges of photon energy and emission angles from a core level derived from a specific atomic site. The resulting intensity I exhibits oscillations as a function of photoelectron wave vector $\mathbf{k}$ due to diffraction and interference effects. This function $I(\mathbf{k})$ can be interpreted as a hologram. Inversion of $I(\mathbf{k})$ using a suitable algorithm, often referred to as a holographic transform, yields a real-space three-dimensional image of the atomic structure near the emitting atom with each neighbouring atom represented by an intensity maximum.

Experimental limitations stipulate discrete sampling of the hologram over a finite region in k space, but the sampling grid must be large and dense enough to yield a clear atomic image.

Depending on the desired resolution, the required data set can involve hundreds or thousands of independent photoemission spectra. Data acquisition can last weeks, and data reproducibility and error can be an issue of concern. Often, the sample surface must be refreshed or regenerated during an experiment to avoid contamination effects. Such sample manipulation or processing tends to introduce a stepwise variation in measured photoemission intensity. Other changes can occur or become necessary during the course of the measurements, such as slit changes, pass energy changes, and synchrotron beam re-injection. Furthermore, it is not unusual that mechanical disturbances to the system such as people bumping the equipment cause stepwise intensity changes. All of these problems can be corrected for with care by intensity renormalization, but the accumulated error over time can still significantly degrade the quality of the final image, which depends on the global precision of the function $I(\mathbf{k})$.

To avoid such problems, it is best to carry out self-normalized measurements. Intensity renormalization then becomes unnecessary, eliminating a major source of error. An additional benefit is a considerable saving in experimental effort. This paper is a discussion of two methods developed recently [11–15]. One of them is based on measurements of core-level spin–orbit branching ratios. Such ratios are independent of the incident synchrotron beam intensity and detector efficiency, and are fairly reproducible from sample to sample (even though the intensity itself may vary significantly). The other method is based on measurements of the logarithmic derivative of the intensity, which is especially useful in cases where the spin–orbit splitting is too small for precise determination of the branching ratio. This quantity is similarly insensitive to changes in experimental parameters. The two methods are, in fact, very similar and closely related.

This paper begins with a brief review of the basics of photoelectron holography as implemented in our studies. The problems associated with precise intensity measurements are illustrated with examples. The two methods of intensity self-normalization are introduced, compared, and verified with recent experimental results for As-terminated Si(111). These methods are also applied to Bi-terminated Si(111), for which there has been a long-standing debate regarding the correct structure. The holographic methods are able to resolve this issue.

2. Basis of photoelectron holography

The basic idea of photoelectron holography is that the direct photoelectron wave emanating from an atom can be scattered by nearby atoms. All of these waves arrive at the detector, and interference gives rise to sinusoidal modulations in the measured intensity I as a function of photoelectron momentum $\mathbf{k}$. Figure 1 illustrates the geometry. Here, $\mathbf{r}_j$ represents the position vector of the jth neighbour relative to the emitter. The geometrical path length difference between the direct wave and the wave scattered off atom j is $r_j - \hat{\mathbf{k}} \cdot \mathbf{r}_j$. Interference between these two waves leads to an intensity modulation of the form $\cos(kr_j - \mathbf{k} \cdot \mathbf{r}_j + \phi)$, where ϕ is the electron scattering phase shift function. The amplitude of such modulation is typically on the order of 10% of the total emission intensity. Data analysis involves extracting this modulation, followed by a holographic transform to obtain the set of vectors $\mathbf{r}_j$.

In the so-called scanned-energy mode of photoelectron holography, the core level intensity I is measured over a set of closely spaced photon energies $h\nu$ for a fixed emission direction $\hat{\mathbf{k}}$. The results, expressed as a function of the photoelectron wave vector k, yield a discretely sampled $I(k, \hat{\mathbf{k}})$. Diffraction modulation is extracted to yield the intensity fine structure function $\chi(k, \hat{\mathbf{k}})$:

$$\chi(k, \hat{\mathbf{k}}) = \frac{I(k, \hat{\mathbf{k}}) - I^0(k, \hat{\mathbf{k}})}{I^0(k, \hat{\mathbf{k}})} \propto \sum_j A_j \cos(kr_j - \mathbf{k} \cdot \mathbf{r}_j + \phi) + \cdots \tag{1}$$
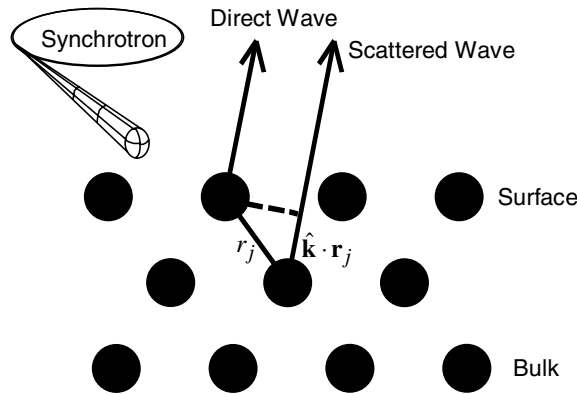
Figure 1. A schematic diagram illustrating the photoemission geometry and the path length difference between the direct photoemission wave and a wave scattered by the jth neighbour.

where I^0 is a smooth background function usually approximated by a low-order polynomial fit to I, and A_j is the scattering amplitude associated with the jth emitter. Atomic cross section variations and crystal field effects are the major contributing factors to the $\boldsymbol{k}$ dependence of I^0.

The measurement of χ is repeated for many emission directions to yield $\chi(\boldsymbol{k})$ over a dense, three-dimensional grid in k space. The image function is obtained by the holographic transform

$$U(\boldsymbol{r}) = \left| \int\int\int \chi(\boldsymbol{k}) \exp(\mathrm{i}\boldsymbol{k}\cdot\boldsymbol{r} - \mathrm{i}kr - \mathrm{i}\phi) g(\boldsymbol{k})\, \mathrm{d}\boldsymbol{k} \right|^2 \tag{2}$$

where $g(\boldsymbol{k})$ is a window function. The numerical integration is usually carried out first over k, and then over the angles. Under the ideal conditions that $g(\boldsymbol{k}) \equiv 1$, the data are continuously sampled over the entire k space, $\phi = \text{constant}$ and the scattering amplitude $A = \text{constant}$, it is straightforward to show

$$U(\boldsymbol{r}) \propto \sum_j A_j^2 \delta(\boldsymbol{r} - \boldsymbol{r}_j). \tag{3}$$

Thus, the image consists of a set of delta functions centred about neighbouring atoms. The prefactors of these delta functions decay rapidly as a function of r_j due to inelastic scattering attenuation and wave expansion, and usually only the first nearest neighbours are detected. Because the form of the kernel in the transform in equation (2) has rather low symmetry, multiple scattering contributions are negligible except in rare pathological cases, and twin images are absent [3, 4, 15].

Data from a real experiment never cover the entire k space, and a window function is necessary. In our case, we employ a product of a Gaussian for the angular window function and a Welch function for the k window function. Each has a smooth cutoff to avoid ringing due to truncation of the Fourier-like integral. This reduction in k space integration results in broadening of the delta functions into intensity maxima with a finite width in real space governed by the uncertainty principle, and weak satellite or ghost features can appear.

The scattering amplitude A and phase shift ϕ can depend on $\boldsymbol{k}$, and are generally unknown. They depend on the scatterer identities and positions $\boldsymbol{r}_j$ which are yet to be determined. The $\boldsymbol{k}$ dependence of A is much less of a concern than that for ϕ. The phase shift problem is similar to that in EXAFS [16–18]. In principle, a self-consistent or recursive analysis can

be performed. However, to keep the method simple and straightforward, most authors opt for a simple sweeping cone approximation [2–5]. In this approach, the angular window function is set to be an angular Gaussian centred about $-\hat{r}$. Each direction $\hat{r}$ in the image function is thus associated with a different angular cone, which is always centred about the backscattering direction. Since the scattering amplitude A has a broad maximum in the backscattering direction, an appropriately chosen sweeping cone limits the integration to this important contribution. The k dependence of the backscattering amplitude is generally slowly varying compared to diffraction modulation and can be neglected. The phase shift is stationary in the backscattering direction, and the angular phase variation within a small cone can be neglected. In evaluating equation (2), the phase shift ϕ is thus replaced by a calculated backscattering phase shift function $\phi(k)$ [19–21], or in cases where the k dependence of the back scattering phase shift is known to be insignificant, by a constant (zero). Thus, equation (3) remains approximately valid, but the limited range of integration causes the delta functions to broaden.

Setting ϕ to zero has the appeal of simplicity, and this approximation is often adopted. In many cases, the k dependence of ϕ is approximately linear over the data range, or $\phi(k) \approx ak + b$. Within the small cone approximation, $\boldsymbol{k} \cdot \boldsymbol{r} \approx -kr$, and the kernel in equation (2) becomes

$$\exp(i\boldsymbol{k} \cdot \boldsymbol{r} - ikr - i\phi) \approx \exp[-2ik(r + a/2)]\exp(-ib). \tag{4}$$

Upon taking the absolute value in equation (2), the $\exp(-ib)$ factor becomes unity and does not contribute to the image. If ϕ is ignored in equation (2), the backscattering bond length extracted from the holographic transform becomes $r_j + a/2$ instead of r_j. Such bond length error is familiar from EXAFS theory [16–18].

In the forward scattering direction, the scattering amplitude is a maximum, and the phase shift is stationary as well. The peaking of the scattering amplitude in the forward direction is known as the forward-focusing effect, and can be utilized to determine interatomic bond directions. However, $kr_j - \boldsymbol{k} \cdot \boldsymbol{r}_j = 0$ for forward scattering, and the intensity data contain little geometric information derived from interference. There is some residual modulation from the $\cos(kr_j - \boldsymbol{k} \cdot \boldsymbol{r}_j + \phi)$ term resulting from a finite angular cone, but this is minimal at low photoelectron kinetic energy ranges typically employed in photoelectron holography. Thus, the forward-focusing effect, while important at high kinetic energies, is generally not utilized for holography. Because of the use of a backscattering cone in our analysis, scatterers above the emitter do not contribute to the final image.

When a photoelectron leaves the surface, it undergoes refraction by the crystal inner potential, which is the leading (constant) term in the Fourier expansion of the crystal potential. This leads to bending of the beam and can cause image shift by a fraction of an Ångstrom. The magnitude of the inner potential is generally not precisely known, but is typically on the order of 10 eV. If a precision on the order of 0.1 Å is considered satisfactory for the image, a nominal value of 10 eV for the inner potential can be used if no other information is available.

The extent and density of the sampling grid in k space, the choice of the cone angle and the inner potential had a direct bearing on the image quality and accuracy. The phase shift problem, or the use of a small cone, further limits the image resolution. It is straightforward to carry out numerical simulations to determine or estimate these effects. Typically, holographic methods are limited to a resolution of about 1 Å. This is often sufficient to determine the overall bonding structure or to single out the correct model from a set of competing models. For a more precise determination of the geometry, a least-square refinement of a model based on the holographic results can be performed, as in LEED analyses [22].
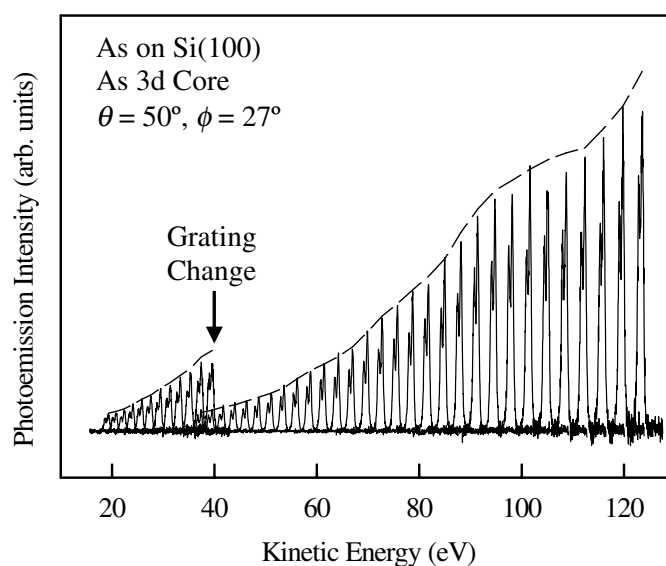
As on Si(100)
As 3d Core
$\theta = 50°$, $\phi = 27°$

Grating
Change

Figure 2. Photoemission spectra of the As 3d core as a function of photoelectron kinetic energy for As on Si(1 0 0) obtained at various photon energies. The emission angles are indicated. The dashed curve shows the intensity variation. The arrow indicates an intensity jump due to grating change.

3. Differential measurements and intensity self-normalization

3.1. Errors in intensity measurements

Figure 2 is an example illustrating a problem with intensity measurements. It displays a set of As 3d core level spectra for a monolayer of As adsorbed on Si(10 0) taken at various photon energies for a particular emission direction as indicated. Diffraction intensity modulation as a function of kinetic energy is evident. A finite jump in the measured intensity noted in the figure is caused by grating change during the experiment to cover different photon energy ranges. The last two spectra taken with a low-energy grating were repeated after the changeover to a high-energy grating. A comparison of the two spectra before and after the grating change yields an intensity renormalization factor that can be used to splice the two sets of data together. Each renormalization generates a small error, which can propagate and accumulate as more such renormalization steps are taken.

Figure 3 is another example, and displays the measured intensity from the As 3d core for a monolayer of As adsorbed on Si(1 1 1). Again, diffraction modulation is evident, and a finite jump in the data is caused by synchrotron beam re-injection. These data points have been normalized to the reading of a synchrotron beam intensity monitor located just before the sample and should be insensitive to beam intensity changes. Nevertheless, the trace shows a jump, which is likely caused by a change in beam position or beam size. In this experiment, the last data point before the re-injection was repeated afterwards to establish a scaling factor in order to splice the two sets of data together. But again, this can cause error, and such repeating measurements take time.

As mentioned earlier, diffraction intensity modulations are often on the order of 10%, and so $\chi \approx 10\%$. To obtain a reasonable image (with a 10% error), the uncertainty in χ should be less than about 10%. Thus, the uncertainty in measured intensity should be less than 1%. This
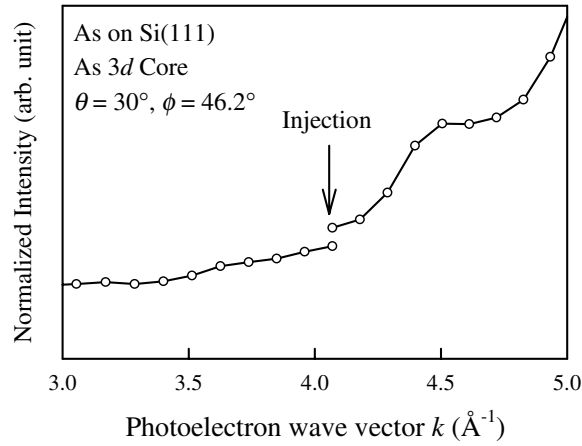
Figure 3. Photoemission intensity of the As 3d core as a function of photoelectron momentum for As on Si(111). The data points (circles) have been normalized by the reading of a synchrotron beam intensity monitor. The curve connects the data points. A jump in intensity indicated in the figure is caused by storage ring re-injection.

level of precision and/or reproducibility is not easy to achieve. Reproducibility is especially problematic if sample surface regeneration is involved. Intensity self-normalization methods, to be discussed below, avoid these problems [11–15].

3.2. Derivative photoelectron holography

The logarithmic derivative of the intensity, $L(k, \hat{\boldsymbol{k}})$, is determined as a function of k for a given emission direction $\hat{\boldsymbol{k}}$. A differential measurement involving two successive spectra with a small difference in photon energy (or photoelectron wave vector) is carried out to yield

$$L(k, \hat{\boldsymbol{k}}) \equiv \frac{I'(k, \hat{\boldsymbol{k}})}{I(k, \hat{\boldsymbol{k}})} = \frac{I\left(k + \frac{\Delta k}{2}, \hat{\boldsymbol{k}}\right) - I\left(k - \frac{\Delta k}{2}, \hat{\boldsymbol{k}}\right)}{\frac{1}{2}\left[I\left(k + \frac{\Delta k}{2}, \hat{\boldsymbol{k}}\right) + I\left(k - \frac{\Delta k}{2}, \hat{\boldsymbol{k}}\right)\right]\Delta k}. \tag{5}$$

This depends on the ratio between the two measured intensities and is thus insensitive to the incident beam intensity and detector efficiency, as long as the relevant experimental conditions are kept constant during the measurement of the two spectra. Global precision of intensity measurement is thus unnecessary. The intensity function itself can be deduced by integration (apart from an unimportant integration constant):

$$I(k, \hat{\boldsymbol{k}}) = \exp\left(\int L(k, \hat{\boldsymbol{k}}) \, \mathrm{d}k\right). \tag{6}$$

The rest of the holographic inversion procedure is the same as discussed above.

Alternatively, one could subtract a smooth background function from $L(k, \hat{\boldsymbol{k}})$ to highlight the oscillatory part due to diffraction. The result is a fine structure function for the logarithmic derivative

$$\zeta(k, \hat{\boldsymbol{k}}) = L(k, \hat{\boldsymbol{k}}) - L^0(k, \hat{\boldsymbol{k}}). \tag{7}$$

From equations (1), (5) and (6), it is straightforward to show

$$\chi(k, \hat{\boldsymbol{k}}) = \exp\left(\int \zeta(k, \hat{\boldsymbol{k}}) \, \mathrm{d}k\right) - 1. \tag{8}$$

Thus, one can deduce χ from ζ without explicit evaluation of I.

3.3. Branching ratio photoelectron holography

Spin–orbit splitting of a core level can give rise to two resolvable photoemission peaks with slightly different values of k. Each spectrum actually contains two measurements, and the branching ratio between the two peaks is independent of the incident beam intensity and detector efficiency. We adopt the following definition for the branching ratio:

$$B(k, \hat{\boldsymbol{k}}) \equiv \frac{I_{l-\frac{1}{2}}(k - \Delta k, \hat{\boldsymbol{k}})}{I_{l+\frac{1}{2}}(k, \hat{\boldsymbol{k}})} \tag{9}$$

where l is the orbital angular momentum, $l \pm \frac{1}{2}$ are the total angular momenta and Δk is the difference in k between the two components. Each spin–orbit-split component shows diffraction modulation. Since there is a slight offset in k, these modulations do not cancel out when the branching ratio is taken. This ratio is related to the derivative of the intensity function as in the previous case.

The modulations in B can be extracted to yield a branching-ratio fine structure function ξ defined below

$$\xi(k, \hat{\boldsymbol{k}}) = \frac{B(k, \hat{\boldsymbol{k}}) - B^0(k, \hat{\boldsymbol{k}})}{B^0(k, \hat{\boldsymbol{k}})} \tag{10}$$

where B^0 is a smooth background function. This can be related to the χ function. From equation (1), $I = I^0(1 + \chi)$, and equation (9) can be rewritten as

$$B(k, \hat{\boldsymbol{k}}) = \frac{I^0_{l-\frac{1}{2}}(k - \Delta k, \hat{\boldsymbol{k}})[1 + \chi(k - \Delta k, \hat{\boldsymbol{k}})]}{I^0_{l+\frac{1}{2}}(k, \hat{\boldsymbol{k}})[1 + \chi(k, \hat{\boldsymbol{k}})]} = B^0(k, \hat{\boldsymbol{k}}) \frac{1 + \chi(k - \Delta k, \hat{\boldsymbol{k}})}{1 + \chi(k, \hat{\boldsymbol{k}})}. \tag{11}$$

Substituting this into equation (10), one obtains

$$\xi(k, \hat{\boldsymbol{k}}) = \frac{B(k, \hat{\boldsymbol{k}})}{B^0(k, \hat{\boldsymbol{k}})} - 1 = \frac{1 + \chi(k - \Delta k, \hat{\boldsymbol{k}})}{1 + \chi(k, \hat{\boldsymbol{k}})} - 1 = \frac{\chi(k - \Delta k, \hat{\boldsymbol{k}}) - \chi(k, \hat{\boldsymbol{k}})}{1 + \chi(k, \hat{\boldsymbol{k}})}. \tag{12}$$

The difference in the numerator can be expanded to yield

$$\xi = \frac{-\Delta k \chi' + 1/2(\Delta k)^2 \chi'' + \cdots}{1 + \chi}. \tag{13}$$

Thus, to first order in Δk,

$$\xi(k, \hat{\boldsymbol{k}}) = -\Delta k \frac{\chi'(k, \hat{\boldsymbol{k}})}{1 + \chi(k, \hat{\boldsymbol{k}})}. \tag{14}$$

Solving this first-order differential equation yields

$$\chi(k, \hat{\boldsymbol{k}}) = \exp\left(-\int \frac{\xi(k, \hat{\boldsymbol{k}})}{\Delta k} \, dk\right) - 1. \tag{15}$$

This equation is very similar to equation (8), which is not surprising because the two methods are closely related. Once $\chi(\boldsymbol{k})$ is deduced, the rest of the calculation is the same as the traditional holographic method. Unlike the derivative method, the quantity Δk here depends on k, and is determined by the spin–orbit splitting.

The branching ratio (and the intensity function itself) can exhibit at least two types of modulations. In addition to the diffraction modulation discussed so far, atomic cross section variations and crystal field effects can give rise to pronounced angular patterns [23, 24]. These patterns are generally slowly varying in angle, and the effects are mostly eliminated by the use of a small backscattering cone [15].
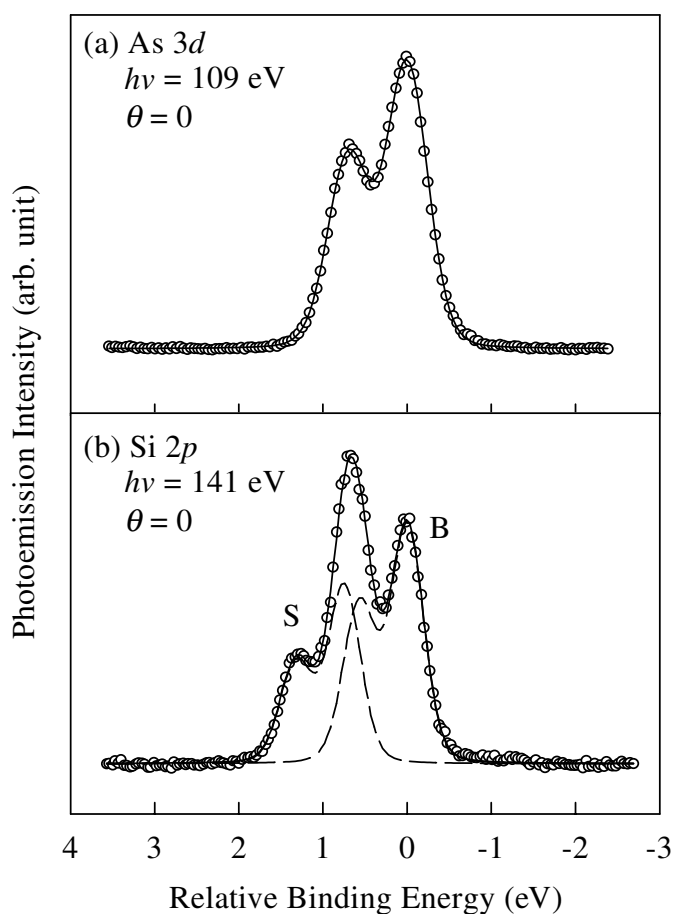
Figure 4. Typical photoemission spectra from As/Si(111)-(1 × 1) for (a) the As 3d core and (b) the Si 2p core. Circles are data points and curves are fits. These spectra were taken with a normal emission geometry ($\theta = 0$). The Si 2p core is decomposed into the surface (S) and bulk (B) components.

4. Experimental results

Our photoemission measurements were carried out at the 1 GeV storage ring Aladdin at the Synchrotron Radiation Center (Stoughton, WI). Several beamlines were used for data acquisition. Each system required at least a week, and more typically two or more weeks of beam time. A hemispherical analyser with a full acceptance cone angle of $\pm 1.5°$ was employed in the measurements. Each core level spectrum was fitted using Voigt lineshapes to represent individual core level components, from which the peak intensities and branching ratios are deduced.

4.1. As on Si(111)

We will begin with a discussion of As terminated Si(111) [14, 15]. The structure of this system is a bulk-terminated Si(111) with the top layer replaced by As forming a (1 × 1) adlayer. Its simple structure makes it an ideal test case. Figure 4 shows some typical spectra taken from both the Si 2p and the As 3d core levels. The As spectrum shows two spin–orbit-split peaks,
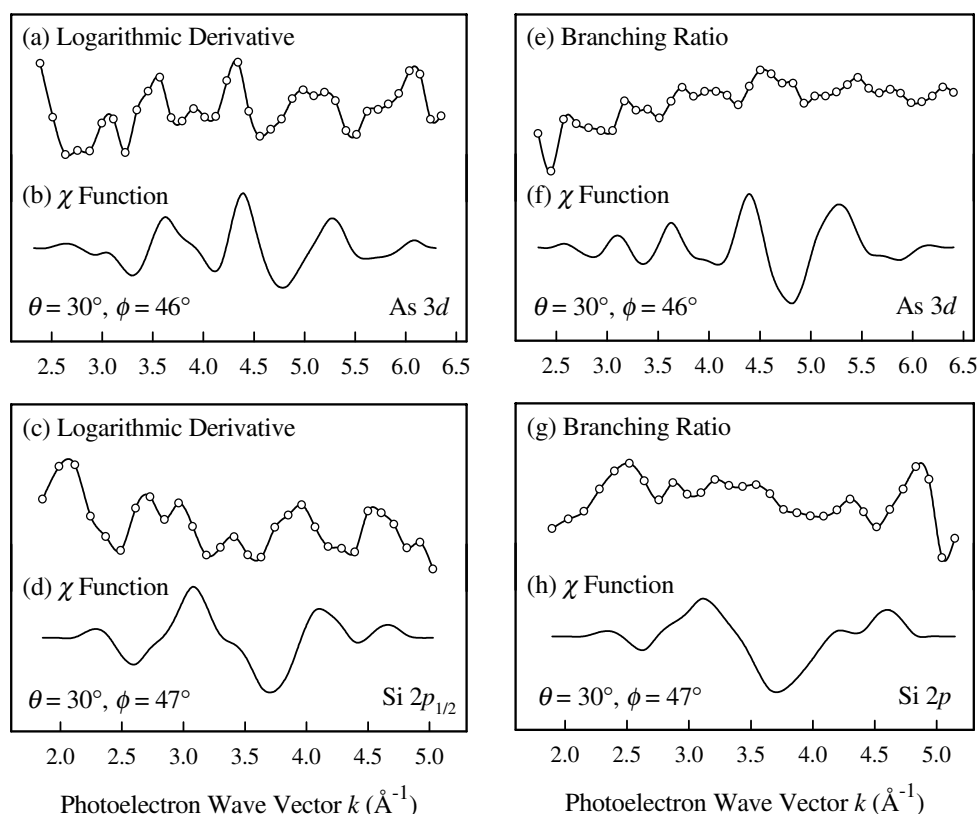
Figure 5. Results for As/Si(111): (a) logarithmic derivative of the As 3d intensity and (b) the corresponding χ function as a function of photoelectron wave vector for a polar angle $\theta = 30°$ and an azimuthal angle $\phi = 46°$; (c) logarithmic derivative of the chemically shifted Si $2p_{1/2}$ intensity and (d) the corresponding χ function as a function of photoelectron wave vector for $\theta = 30°$ and $\phi = 47°$. The corresponding results based on branching ratio measurements are shown in (e)–(h).

while the Si spectrum shows two sets of spin–orbit-split peaks. As labelled in the figure, one of them (labelled S for surface) is derived from the top layer of Si directly bonded to the surface As, and the other (labelled B for bulk) is derived from the rest of the Si crystal. The S component has a significantly larger binding energy, and the chemical shift is caused by direct bonding to the highly electronegative As.

For the As 3d core level, 38 spectra evenly spaced in k within the range of 2.4 Å^{-1} < k < 6.4 Å^{-1} were measured for each of 44 different emission directions roughly evenly spaced over a polar angle range of $\theta = 0°$ to 70° and an azimuth angle range of $\phi = 0°$ to 60° ($\phi = 0$ corresponds to $[2\bar{1}\bar{1}]$). Threefold rotation and mirror symmetry operations expanded the effective number of angles to 238, corresponding to a total of more than 8800 points in k space. A similar set of data from the Si 2p core level was also taken. The branching ratio is directly determined from a least-squares fit to each spectrum. The logarithmic derivative is obtained by doing the necessary calculations using a pair of spectra. During the measurement of a pair, care was taken not to change or disturb the system; in other words, slit changes, grating changes, ring re-injection etc, were not allowed, and data were simply discarded if any accidental mechanical disturbances occurred.

The upper-left panel in figure 5 shows a logarithmic derivative function derived from the As 3d core level for an arbitrarily chosen emission direction. The corresponding χ function

deduced from equation (8) is also shown. The upper-right panel shows a branching ratio function and the corresponding χ function deduced from equation (15) for the same core and the same emission direction. The two methods should yield the same χ function. A comparison shows that the χ functions deduced from the two methods are indeed very similar. The maxima and minima occur at the same energies. The differences in peak heights can be attributed to experimental uncertainties (data noise) and systematic errors (higher order terms ignored in the analytical formula). Both the experimental uncertainties and systematic errors are on the order of 1% in I, or $\sim$10% in the χ function. The discrepancies in peak height are less of a problem since only the oscillation periods are relevant to the atomic positions. The two lower panels in figure 5 provide a similar comparison for the chemically shifted Si 2p core for an arbitrary chosen emission direction. Again, the derived χ functions show good agreement in the positions of the maxima and minima.

The image functions derived from the two methods are shown in figure 6. The results based on the derivative (branching ratio) method are presented on the left (right). Displayed in this figure are planar slices through the image functions. The first three images in each case are derived from the As 3d core level, and the bottom panel is derived from the chemically shifted Si 2p core level. Shown in the middle are ball–stick models with the emitter and the slicing planes indicated. The structure, as discussed earlier, is a bulk terminated Si lattice with the top layer replaced by As. The crosses in each image indicate the expected positions of scattering atoms based on an average of available theoretical and experimental results. Stars indicate the position of the origin of the image function (position of the emitter).

Figures 6(a) and (e) show a vertical slice through the As emitter and one of the three pedestal Si atoms. The images show the pedestal atom as a bright intensity maximum. Below this atom, one can also see the Si atom bonded in the layer below. The intensity associated with this second-layer Si atom is dimmer due to inelastic scattering attenuation and wave expansion. In each of these two images, there is also a very weak, barely visible feature on the left-hand side, which can be attributed to a ghost due to the approximations employed in the holographic analysis.

Figures 6(b) and (f) show images in a horizontal slice across the three pedestal Si atoms, and the three atoms are clearly visible. In addition, there is a faint ring-like feature in between the three atoms. This is the same ghost feature mentioned above. Figures 6(c) and (g) are horizontal slices across the second layer of Si atoms below the As. Since the intensities are lower, the images have been amplified by a factor of 1.5 to show details. The bottom images in figure 6 are derived from the chemically shifted Si 2p core. The emitter position is different from that in the previous images, and the results show the Si atom in the second layer directly underneath the emitter in agreement with the model. Since forward scattering is not included in the analysis, the As atom above does not appear in the image.

These results demonstrate an excellent agreement between the branching ratio and the derivative results. The atomic positions in the holographic images are also in good agreement with the average positions determined in previous experimental and theoretical studies. The discrepancy is less than $\sim$0.2 Å. This experiment was designed for an accuracy of $\sim$10% in the χ function, which translates into a $\sim$0.2 Å accuracy in bond length for the first neighbours.

4.2. Bi on Si(111)

Most of the photoelectron holography work to date has dealt with simple model systems with a known structure, and the purpose has been to demonstrate that the method works. It would be interesting to apply photoelectron holography to cases where the structure is unknown, or where the structure is controversial based on other experimental results. Bi on Si(111) is one
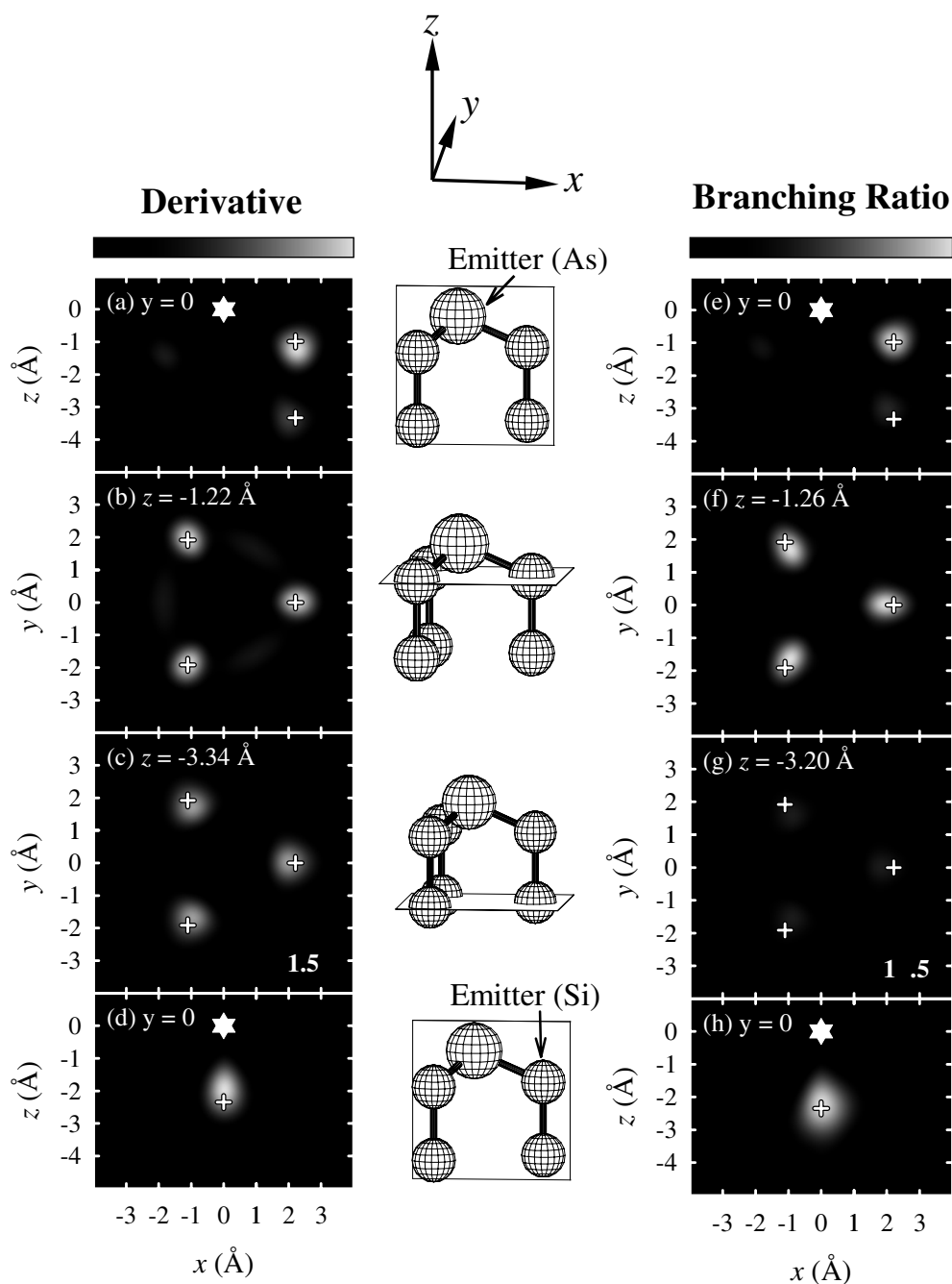
Figure 6. Planar slices of the image function for As/Si(111) through various atomic planes as indicated in the accompanying ball–stick model drawings. The grey scales used for image presentation are indicated near the top of the figure by a linear mapping of the intensity levels into grey levels. (a)–(d) are results based on the logarithmic derivative method, and (e)–(h) are results based on the branching-ratio method. In each case, the top three panels are images obtained from the As 3d data, and the bottom panel is an image obtained from the Si 2p data. The intensity level for images (c) and (g) has been amplified by a factor of 1.5 to improve visibility.
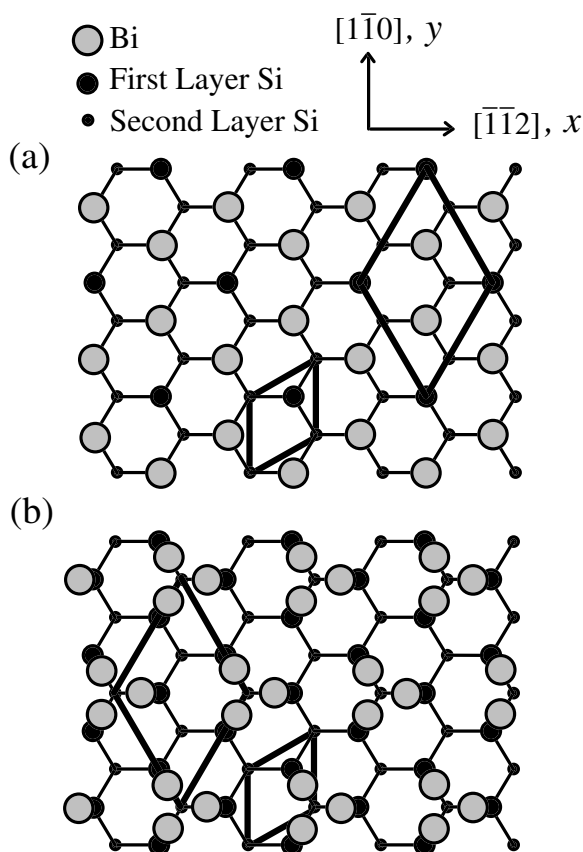
Figure 7. Structural models for Bi on Si(111): (a) the honeycomb model and (b) the trimer model viewed from above. The coordinate system is indicated. The (1×1) and $(\sqrt{3} \times \sqrt{3})R\,30°$ unit cells are outlined.

of those simple adsorbate systems for which there has been considerable debate about the structure.

This system exhibits a $(\sqrt{3} \times \sqrt{3})R\,30°$ reconstruction for a range of Bi coverage near one monolayer (ML). Numerous studies have yielded two competing models: (i) a honeycomb model with an ideal coverage of two-thirds of ML, in which the Bi atoms are located in the on-top T_1 sites directly above the top layer Si atoms; and (ii) a trimer model with an ideal coverage of one ML, in which the Bi atoms are laterally displaced from the T_1 sites to form trimers. These two models are displayed in figures 7(a) and (b), respectively. The key question is whether or not this lateral displacement is zero, which sets these two models apart. Because this displacement averages to zero over a trimer unit, this is a relatively difficult problem for standard diffraction methods. The holographic technique is ideally suited for such a situation.

Both the derivative method and the branching ratio method have been applied to this system [11, 12]. The results are very similar. Only the images from the derivative method are presented here. Figure 8(a) is a vertical slice through the Bi emitter (the origin) in an xz plane. If the honeycomb model were correct, we would expect to see a single intensity maximum below the origin corresponding to the Si atom bonded directly underneath the Bi. Instead, there are two resolved maxima, with the one on the right being more intense. A horizontal
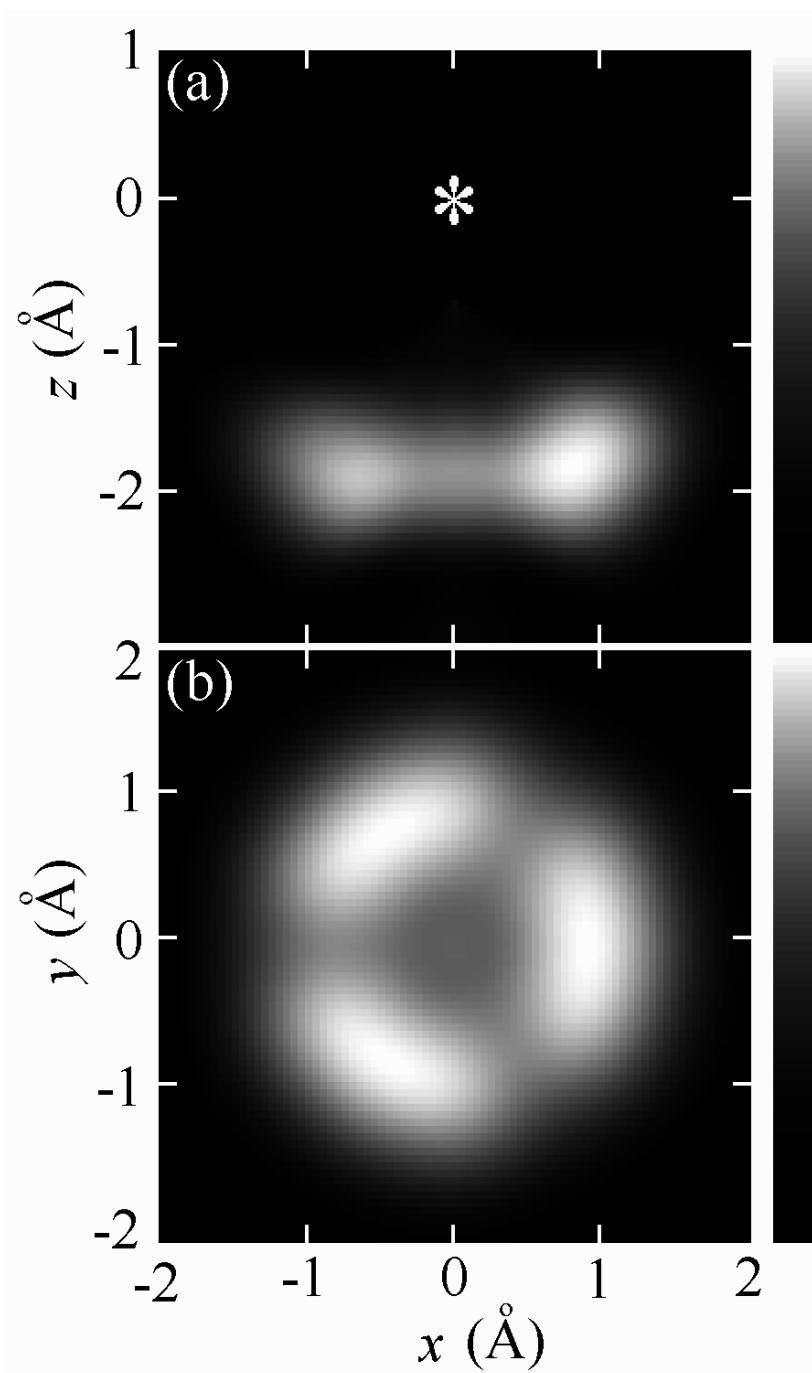
Figure 8. (a) A vertical and (b) a horizontal planar slice through the image function for Bi/Si(111). The coordinate system is as defined in figure 7, and the origin, indicated by a star in (a), is at the emitter position.

slice of the image function in an *xy* plane through these maxima is shown in figure 8(b). Three intensity maxima are present in this plane forming an equilateral triangle. This rules out the honeycomb model.

For the trimer model, each Bi adatom has one Si atom bonded below it and offset to one side. The three Bi atoms in a trimer unit each gives rise to an intensity maximum, and the final holographic image is a sum of the three separate images, and should exhibit three intensity maxima. This is exactly what the holographic images show. In addition, the orientation of the three intensity maxima in figure 8(b) agrees with the crystallographic orientation as illustrated in figure 7(b), which was verified by x-ray diffraction. The intensity maximum in figure 8(a) on the right corresponds to one of the three Si atomic positions, and the less intense maximum on the left corresponds to the saddle point in between the other two Si atomic positions. These results confirm that the trimer model represents the correct structure.

5. Summary and concluding remarks

Photoelectron holography has emerged as a powerful method for model-independent determination of surface structure, and for sorting out competing models that are difficult to distinguish by other techniques. However, such experiments require a large data set with high precision, and maintaining the required precision over the entire data set can be difficult. This paper reviews two methods that avoid the need for global precision in intensity measurements. These are the logarithmic derivative method and the branching ratio method. Both of these methods are based on intensity self-normalization, and the results are thus independent of the incident beam intensity and detector efficiency. Using As/Si(111) as an example, we show that the two methods yield the same and correct atomic structure. These methods are also employed to clarify the highly debated structure of Bi/Si(111).

The concept of intensity self-normalization and differential measurements is not necessarily limited to the two methods presented here. There is a large literature on photo-electron diffraction and holography based on angular patterns in intensity and branching ratio. Differential measurements involving small angular changes can be similarly employed to construct a hologram. Another possibility is to modulate the incident synchrotron beam polarization state as in ellipsometry or dichroism measurements. Such methods might offer additional capabilities or utilities.

References

[1] Barton J J 1991 *Phys. Rev. Lett.* **67** 3106
[2] Wu H, Lapeyre G J, Huang H and Tong S Y 1993 *Phys. Rev. Lett.* **71** 251
    Wu H and Lapeyre G J 1995 *Phys. Rev.* B **51** 14 549
    Lapeyre G J 1994 *Nucl. Instrum. Methods* A **347** 17

[3] Tong S Y, Wei C M, Zhao T C, Huang H and Li H 1991 *Phys. Rev. Lett.* **66** 60
  Tong S Y, Huang H and Wei C M 1992 *Phys. Rev.* B **46** 2452
  Tong S Y, Li H and Huang H 1992 *Phys. Rev.* B **46** 4155
[4] Tobin J G and Waddill G D 1994 *Surf. Rev. Lett.* **1** 297
  Tong S Y, Li H and Huang H 1994 *Surf. Rev. Lett.* **1** 303
  Heinz K and Wedler H 1994 *Surf. Rev. Lett.* **1** 319
  Wei C M, Hong I H and Chou Y C 1994 *Surf. Rev. Lett.* **1** 335
[5] Sieger M T, Roesler J M, Lin D-S, Miller T and Chiang T-C 1994 *Phys. Rev. Lett.* **73** 3117
[6] Tobin J G, Waddill G D, Li H and Tong S Y 1993 *Phys. Rev. Lett.* **70** 4150
[7] Terminello L J, Barton J J and Lapiano-Smith D A 1993 *Phys. Rev. Lett.* **70** 599
[8] Harp G R, Saldin D K and Tonner B P 1990 *Phys. Rev. Lett.* **65** 1012
[9] Fadley C S 1993 *Surf. Sci. Rep.* **19** 231
[10] Roesler J M, Miller T and Chiang T-C 1996 *Surf. Sci.* **348** 161
[11] Roesler J M, Sieger M T, Miller T and Chiang T-C 1997 *Surf. Sci.* **380** L485
[12] Roesler J M, Miller T and Chiang T-C 1998 *Surf. Sci.* **417** L1143
[13] Luh D-A, Sieger M T, Miller T and Chiang T-C 1997 *Surf. Sci.* **374** 345
[14] Luh D-A, Miller T and Chiang T-C 1998 *Phys. Rev. Lett.* **81** 4160
[15] Luh D-A, Miller T and Chiang T-C 1999 *Phys. Rev.* B **60** 16722
[16] Stern E A 1978 *Contemp. Phys.* **19** 289
[17] Lee P A and Beni G 1977 *Phys. Rev.* B **15** 2862
[18] Teo B-K and Lee P A 1979 *J. Am. Chem. Soc.* **101** 2815
[19] Pendry J B 1974 *Low Energy Electron Diffraction* (New York: Academic)
[20] NIST Elastic Electron Scattering Cross Section Data Base v. 2.0 (National Institute of Standards and Technology 2000) http://www.nist.gov/srd/nist64.htm
[21] Rehr J J and Albers R C 1990 *Phys. Rev.* B **41** 8139
[22] Terborg R, Hoeft J T, Polcik M, Lindsay R, Schaff O, Bradshaw A M, Toomes R, Booth N A, Woodruff D P, Rotenberg E and Denlinger J 2000 *Phys. Rev.* B **60** 10715
[23] Yeom H W, Abukawa T, Takakuwa Y, Fujimori S, Okane T, Ogura Y, Miura T, Sato S, Kakizaki A and Kono S 1998 *Surf. Sci.* **395** L236
[24] Bullock E L, Gunnella R, Natoli C R, Yeom H W, Kono S, Patthey L, Uhrberg R I G and Johansson L S O 1996 *Surf. Sci.* **352–354** 352